RESEARCH PAPER

Effect of Alkali Strength on the Hydrothermal Growth of Photoactive TiO$_2$ Nanowires

Abubakar Hamisu[1,2], Umar Ibrahim Gaya [1] , Abdul Halim Abdullah[3,4]*

[1] *Department of Pure and Industrial Chemistry, Bayero University Kano, 700241 Kano, Kano State, Nigeria*

[2] *Department of Chemistry, Kano University of Science and Technology Wudil, Kano, Nigeria*

[3] *Department of Chemistry, Faculty of Science, Universiti Putra Malaysia, 43400 UPM Serdang, Selangor D.E., Malaysia*

[4] *Institute of Advanced Technology, Universiti Putra Malaysia, 43400 UPM Serdang, Selangor D.E., Malaysia*

ARTICLE INFO

ABSTRACT

Titanium dioxide nanowires have been prepared by the alkali hydrothermal treatment of TiO$_2$ nanoparticles in presence of different hydroxides and characterized using transmission electron microscopy (TEM), scanning electron microscopy (SEM), energy dispersive x-ray (EDX), N$_2$ adsorption-desorption measurements, powder x-ray diffraction (XRD) and UV-Vis spectroscopy. Interestingly, only the strong bases (NaOH and KOH) formed mainly anatase titanium dioxide nanowires with the evident collapse of definitive (110) rutile XRD peak. The KOH-based titanium oxide nanowires exhibited comparatively low diameter (~5 nm), high surface area (228.34 m^2/g), and low band gap energy (2.90 eV), and showed the most remarkable photocatalytic degradation (98.87 %). However, the NH$_4$OH-based titanium dioxides were nanoparticles having insignificantly modified morphology and least photocatalytic efficiency. The effect of operating variables on the degradation of aqueous methylene blue (MB) over the obtained alkali hydrothermal TiO$_2$ was studied using response surface methodology, based on a bivariate central composite design (CCD) and optimized numerically.

How to cite this article

INTRODUCTION

Nanostructured materials exhibit a wide variety of unique properties for application in array of scientific and technological developments such as photocatalysis, sensors, voltaic cells, shielding interference in communication field, reducing electromagnetic radiation and disinfection [1-3]. In photocatalysis, light with sufficient energy causes the formation of conduction band electron and valence band hole (charge carriers) which serve as mini-microreactors for photocatalytic reduction and oxidation. Over the decades, the photo-oxidative degradation of environmentally recalcitrant compounds such as synthetic organic dyes over nanostructured materials has attracted enormous interest. Apart from nano-TiO$_2$ which is currently much referred nano-photocatalyst, a high number of other photoresponsive nanomaterials have been described [4,5]. One advantage immediately obvious from these materials is that they can shorten charge carrier transfer distance due to their smaller particle sizes and larger surface areas which ultimately translates into enhanced photocatalytic activity [6].

Titanium dioxide (TiO$_2$) nanomaterials have attracted considerable attention due to their unusual optical, electronic and mechanical properties [7]. Various shapes of 1D TiO$_2$

* *Corresponding Author Email: uigaya.chm@buk.edu.ng*

nanomaterials such as nanowires, nanowires, nanofibers, nanoribbons, nanobelts, and nanoneedles have been discovered in nanotechnology and used in different applications [8,9]. Aside from the inherent TiO$_2$ characteristics, these materials show relatively faster charge carrier transfer, improved electron/ hole separation, higher active surface area and photoactivity compared to 0D TiO$_2$ nanoparticles [10,11]. Thanks to their large specific surface area, it is easy for photogenerated carriers to transfer along the axial direction [12]. Moreover, they have the ability to capture scattered light, which will increase light harvesting and easier charge carrier separation than TiO$_2$ nanoparticles [13].

Many methods have been successfully established for the fabrication of nanostructured TiO$_2$, including laser ablation, arc discharge, template-assisted synthesis which are inevitably associated with product contamination due to prior use of template or catalyst [14]. Consequently, there is renewed interest to synthesize nanostructured materials devoid of template intervention and some many methods such as solvothermal [15], hydrothermal [16, 17], sol-gel [18], chemical vapor deposition [19], and microwave [20] have been successful. Hydrothermal method is perhaps the the most powerful technique owing to its simplicity, cost-effective, high reactivity, easy control and environmentally safe route, and for these reasons it has been used to prepare a wide range of 1D TiO$_2$ nanostructures including nanowires [21-24]. Unlike TiO$_2$ nanowires, the TiO$_2$ nanowires (TNWs) produced using strong alkali can withstand higher calcination temperature (> 500 °C) without phase change to the anatase polymorph or any change in the nanowire structure [25]. In this work, the hydrothermal synthesis of TNWs using different alkali of different is reported to visualise the effect of these alkali on the product characteristics. The photoactivity of the resulting titanium dioxide was assessed based on the degradation of MB and optimized using response surface methodology.

MATERIALS AND METHODS
Materials
Commercial TiO$_2$ nanopowder (P25, 80% anatase, and 20% rutile) used as precursor material was purchased from Sigma-Aldrich. Methylene blue (MB, 97%) was purchased from Sigma-Aldrich. Potassium hydroxide (KOH, 90%), sodium hydroxide (NaOH, 98%), ammonium hydroxide solution (NH$_4$OH, 30%), and hydrochloric acid (HCl, 37%v/v) were purchased from R & M Chemicals.

Preparation of TiO$_2$ nanowires
To prepare TiO$_2$ nanowires, 1.2 g of Degussa TiO$_2$ was added into three beakers, each containing 20 ml of deionized water. The mixture was magnetically stirred for 30 min and sonicated for the same time period. Subsequently, 20 ml of 10 mg/l NaOH, KOH and NH$_4$OH were separately added dropwise into the mixture under vigorous stirring, followed by sonication for 45 min. Each mixture was autoclaved at 180°C for 24 h. After cooling, white precipitates were filtered and washed several times with 0.1 mg/l HCl and deionized water until neutral pH. These precipitates were dried at 75 °C overnight and then calcined at 450 °C for 4 h. With NaOH and KOH, TiO$_2$ nanowires were obtained (Na/TNW and K/TNW), while NH$_4$OH gave titanium dioxide nanoparticles (NH/TNP).

Characterization
The composition, structure, and morphologies of the synthesized titanium dioxides were analyzed using a NOVA NANOSEM 230 ultra high-resolution field emission scanning electron microscope (FE-SEM) hyphenated with energy dispersive x-ray (EDX) spectrometer, and a JEM-2100F field emission TEM. The X-ray diffraction (XRD) patterns of the synthesized photocatalysts were derived from a Shimadzu XRD-6000 X-ray diffractometer operated with a Cu Kα radiation (λ = 0.15406 nm) in the 2θ range of 20-80°. The Brunauer–Emmett–Teller (BET) method was used to determine the specific surface area and pore volume of the samples. Nitrogen adsorption-desorption experiments were performed using a Micromeritics 3Flex 1.02 instrument at 77.322 K. All the samples were degassed at 200 °C for 2 h before the experiment. The analysis of band gap was performed against a BaSO$_4$ reference, using a Shimadzu UV-3600 UV-VIS-NIR spectrophotometer, within a scan range of 220-800 nm.

Photocatalytic experiments
The photocatalytic performance of the photocatalysts (Na/TNW, K/TNW, and NH/TNP) was evaluated by monitoring the percentage degradation of methylene blue (MB) for 60 min. Experiments were carried out in an immersion

Table 1. Actual values and coded levels of operating variables.

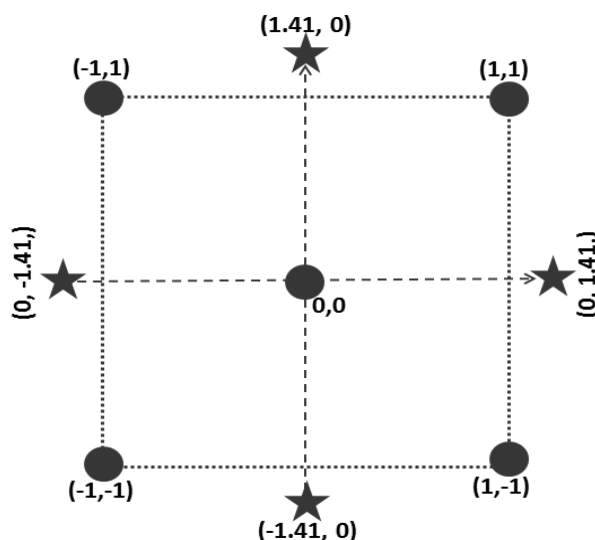| Factor	Actual (and coded) levels				
[TiO$_2$], g/L	0.2 (-1.41)	0.4	0.6 (0)	0.8 (+1)	1 (+1.41)
[MO], mg/L	15 (-1.41)	20	25 (0)	30 (+1)	35 (+1.41)

Fig. 1. Coordinates of the two-factor central composite design.

well photoreactor fitted with a new 3 W China model E14 GMY UV lamp (UV intensity = 450 µw/cm^2, wavelength = 253 nm). In the photocatalytic experiments, a solution containing the desired amount of MB and catalyst was added to the photoreactor. Solution pH was adjusted using NaOH and H$_2$SO$_4$ and oxygen was continuously supplied to the system. Initially, the system was agitated in the dark for 30 min. At periodic intervals of experiment time, test samples were taken, filtered using cellulose nitrate membrane (0.45 µm), and absorbance was read at 664.1 nm using Perkin Elmer Lambda 35 UV-Vis spectrometer. The percentage degradation of the initial MB concentration was calculated using Eq.(1).

$$D\% = \frac{[MB]_o - [MB]_t}{[MB]_0} \times 100 \qquad (1)$$

Where [MB]$_o$ is the initial methylene blue concentration, [MB]$_t$ is the concentration of methylene blue at irradiation time *t*.

The effect of degradation variables of the MB in the presence of the titanium dioxide nanowires (Na/TNW and K/TNW) was studied for 60 min using a Box-Wilson two-factor central composite design (CCD). The independent parameters were TiO$_2$ loading and initial concentration of MB. The CCD consists of three sets of points: center points, factorial points, and axial points. The experimental ranges and the levels (coded and uncoded) of the independent variables that were determined by the preliminary experiments are given in Table 1. The factorial points are located at the vertices of a square with coordinates which are a combination of -1(low value) and +1 (high value). The coordinate of the center points is 0,0. The axial or star points were augmented to the factorial at a distance ± α = 1.41 along with center point to make the design rotatable (as shown in Fig. 1). A total of 11 experiments were performed in this work, including four experiments at the factorial points, four experiments at the axial point, and three replications at central points, as governed by Eq. (2) [26].

$$N = 2^n + 2n + n_c = 2^2 + 2(2) + 3 = 11 \qquad (2)$$

where *N* is the total number of experiments required, *n* is the number of factors and n_c is replications at central points. The degradation efficiency values obtained from the experiment
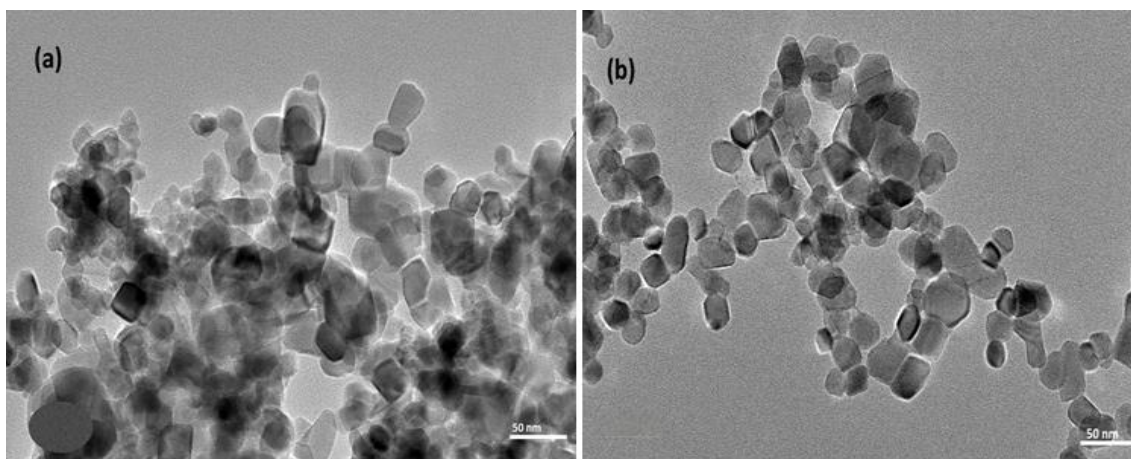
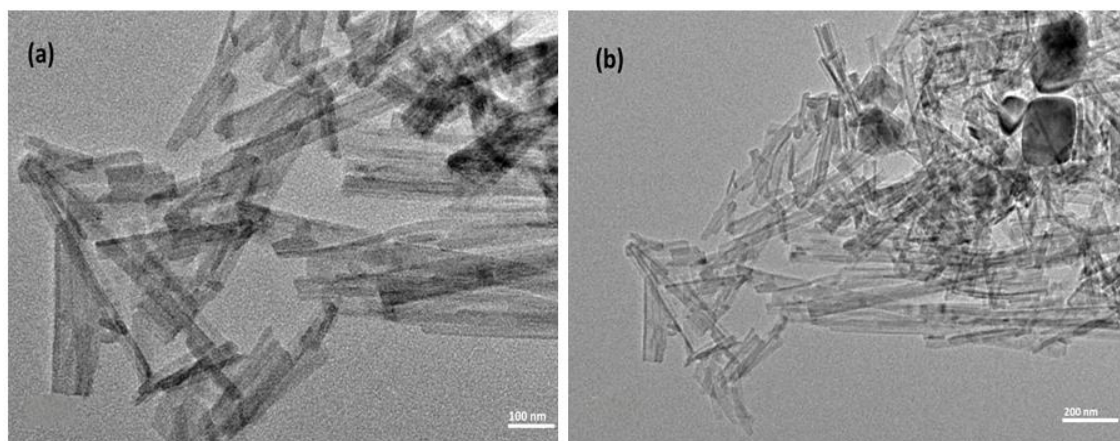Fig. 2. The TEM image of (a) P25 and (b) NH/TNP.

Fig. 3. The TEM image of Na/TNW with different magnification.

(% D) were processed using a response surface module to obtain statistically valid predicted values. Kinetic studies were performed for 100 min and data was fitted to the pseudo-first-order integrated rate equation.

RESULT AND DISCUSSION
TEM, SEM and EDX Analysis

Fig. 2 shows the TEM image for TiO_2 (precursor) and the NH/TNP derived from NH_4OH hydrothermal treatment. It can be seen that the precursor exhibits aggregated particles with an average particle size of 21.8 nm (Fig. 2a) which upon hydrothermal treatment with the weak base, no significant change in the morphology was observed and no nanowire was formed. However, the particle size of the nanoparticles decreased to 18.6 nm (Fig. 2b). Differently, with NaOH and KOH

≈ 367nm long, ≈ 20 nm diameter titanium dioxide nanowires (Na/TNW) (Fig. 3) and ≈ 74 nm long, ≈ 5 nm diameter titanium dioxide nanowires (K/TNW) were formed, respectively (Fig. 4). From the TEM images, it was observed that the size and shape of TNTs strongly depend upon the strength of the alkali employed.

The morphology of the as-prepared titanium dioxides was imaged by field emission SEM (Fig. 5). It can be seen from the images that the NH/TNP does not transform into a nanowire, rather, it appears as a collection of aggregated particles (Fig. 2a). However, the nanowires of the Na/TNW and K/TNW can readily be observed from Fig. 5b and Fig. 5c, respectively. Hence, the SEM results corroborate those of the TEM, revealing that only the strong bases may be used in the hydrothermal synthesis of nanowires. Nonetheless, even with
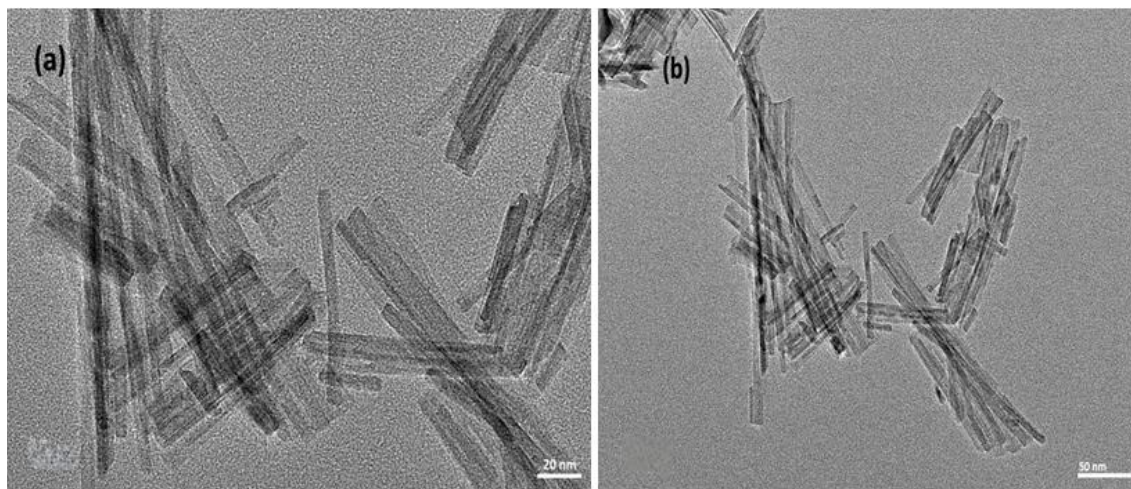
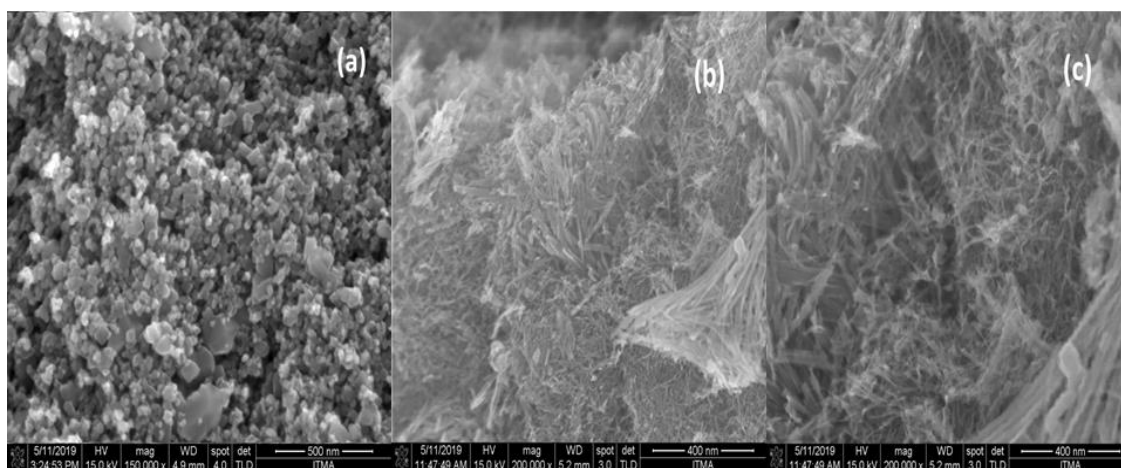Fig. 4. The TEM image of K/TNW with different magnification.

Fig. 5. The FE-SEM image of (a) NH/TNP, (b) Na/TNW and (c) K/TNW.

the strong alkali, some of the resulting nanowires aggregated into bundles, a phenomenon similarly observed by Zhang et al. [27] while synthesizing TiO₂ nanowires.

Compositional analysis of the as-prepared titanium dioxides was performed using energy dispersive x-ray (EDX) spectroscopy. Fig. 6 shows the EDX spectra of NH/TNP, Na/TNW and K/TNW. The EDX spectra of all the three samples show peaks corresponding solely to Ti and O. This observation rules out the presence of impurities in the obtained TiO₂ nanowiresand nanoparticles.

Nitrogen adsorption-desorption measurements

The surface area and pore volume of the hydrothermal titania were estimated using the methods of Brunauer-Emmett-Teller (BET) and Barrett-Joyner-Halenda (BJH). Fig. 7 shows the N_2 adsorption-desorption isotherm, the BET surface area plot (left inset) and the BJH adsorption cumulative pore volume curve (right inset) for P25, NH/TNP, Na/TNW, and K/TNW. The surface area and pore volume of bare P25 were found to be 54.85 m²/g and 0.14 cm³/g, and for NH/TNP, these properties increased to 77.66 m²/g and 0.26 cm³/g, respectively. More interestingly, the Na/TNW and for K/TNW exhibited the highest values of these parameters (143.42 m²/g and 0.46 cm³/g, and 228.34 m²/g and 0.62 cm³/g, respectively), corroborating the fact that the formation of nanowires from TiO₂ particle by the alkali hydrothermal process is associated with
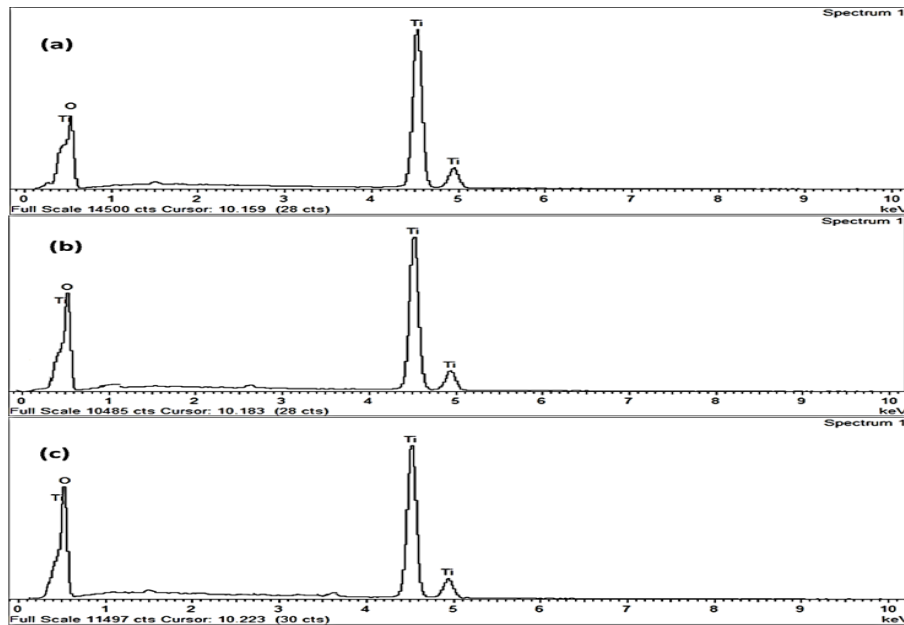
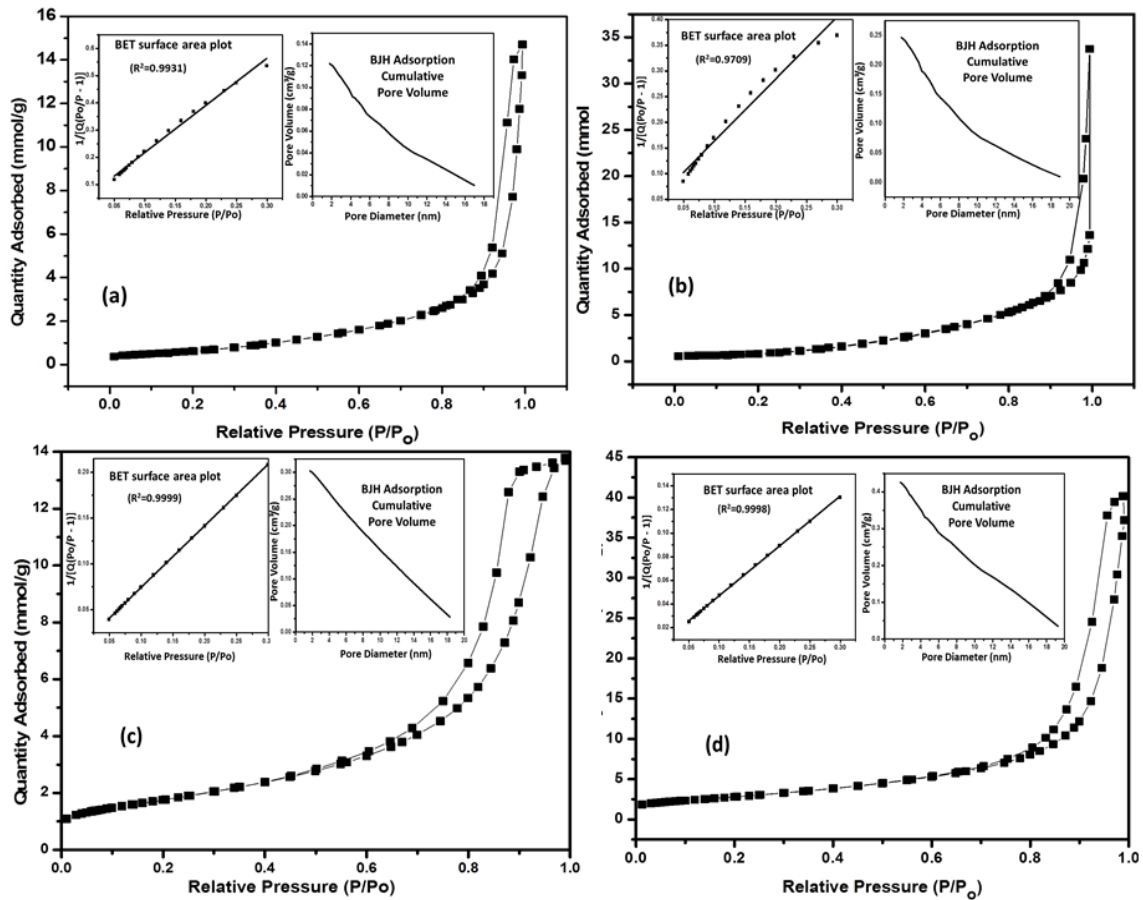Fig. 6. The EDX spectra of (a) NH/TNP, (b) Na/TNW and (c) K/TNW.

Fig. 7. Nitrogen adsorption-desorption isotherms with BET surface area plot (left inset) and BJH adsorption cumulative pore volume curve (right inset) for (a) P25, (b) NH/TNP, (c) Na/TNW and (d) K/TNW.
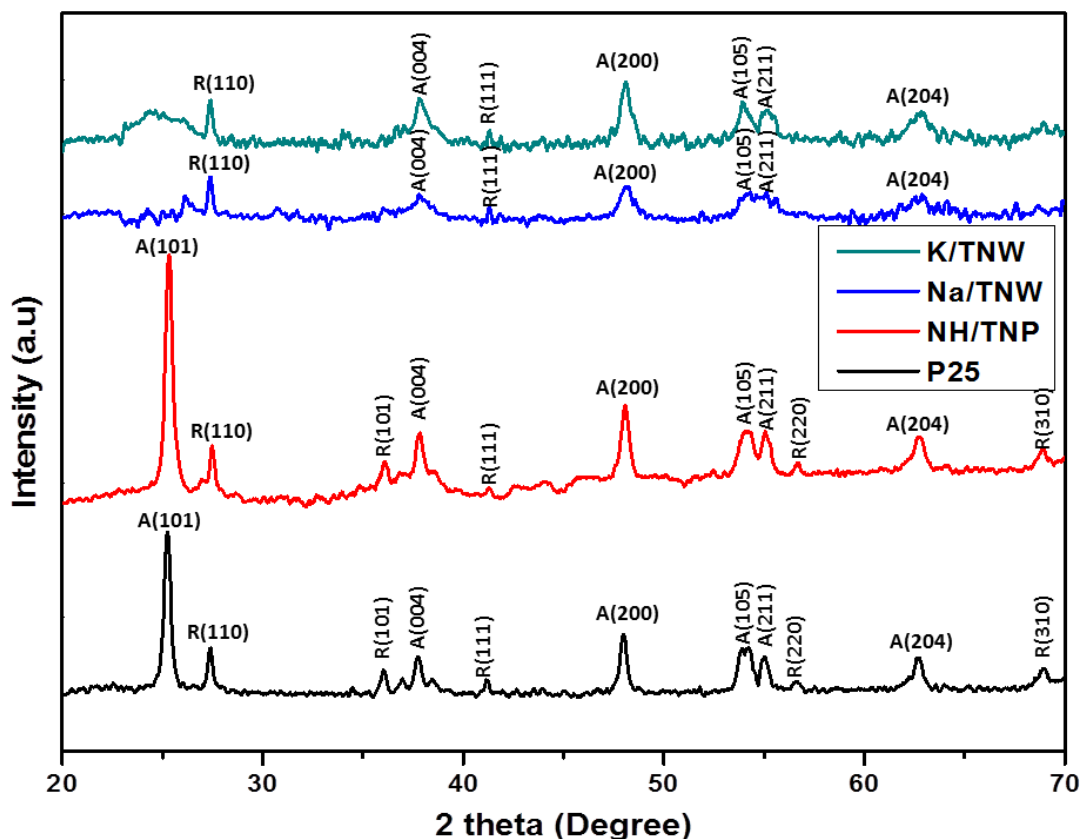
Fig. 8. The XRD patterns of the synthesized catalysts (A = anatase and R = rutile).

significant increase in the surface area and pore volume of the material[22,28]. The Na/TNW (Fig. 7c) and K/TNW (Fig. 7d) showed type IV IUPAC isotherm [29]. Their mesoporosity is confirmed by the presence of hysteresis loops and obvious condensation/evaporation steps within partial pressure range of 0.6 to 0.9 [30] as it generally happens in nanotubular structures[22].

XRD analysis

In order to study the crystalline structures and phase compositions of the prepared catalysts, X-ray diffraction patterns were collected (Fig. 8). By the TEM results, the average crystallite size of P25 was found to be 21.29 nm which decreased to 18.51 nm for NH/TNP. The XRD peaks of the samples were studied by comparison with JCPDS-21-1272 and JCPDS-21-1276. From the figure, P25 and NH/TNP are observed to be more crystalline than the synthesized TNTs. As seen from the figure, P25 (the starting material) and NH/TNP show anatase peaks at 2θ (and planes) = 25.21° (101), 37.80°

(004), 48.02 (200), 54.06° (105), 55.10° (211), 62.71° (204) and rutile peaks 2θ (and planes) = 27.44° (110), 36.09° (101), 41.21° (111), 56.68° (220), 68.87° (310). The Na/TNW and K/TNW show anatase peaks at 2θ (and planes) = 37.82° (004), 48.06° (200), 53.96° (105), 62.73° (204) and rutile peak at 2θ (and planes) = 27.37° (110) and 41.16° (111). The diffraction pattern of the nanowires show mainly anatase polymorph, a little rutile and amorphous mix, with a clear disappearance of the prominent (101) anatase reflection as previously observed by other workers [31,32].

Band gap analysis

To estimate the band gap of the obtained catalysts, reflectance measurements were performed over wavelengths of 220–800 nm. The UV–Vis reflectance spectra are displayed in Fig. 9a while the band gap energies of the photocatalysts, estimated from the widely recommended plot of reflectance function [F(Rα)hv]^2 versus hv [33] are displayed in Fig. 9b. The band-gap energy of P25,
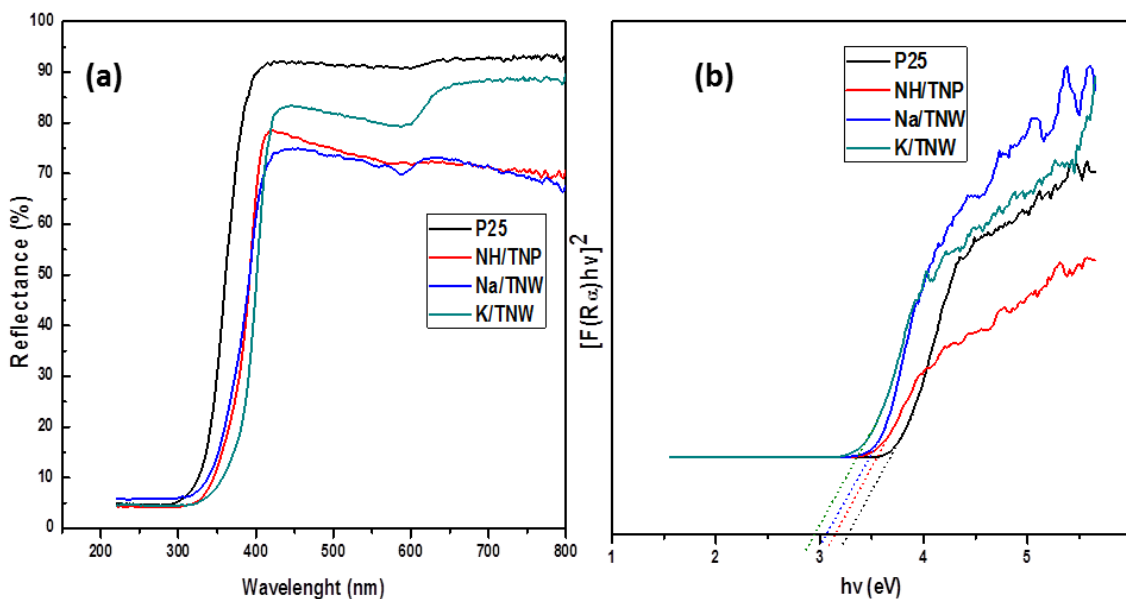
Fig. 9. . (a) UV–Vis reflectance spectra of the samples (b) Plot of (F(R**α**)h**ν**)^2 versus hν of the samples for band gap evaluation.

NH/TNP, Na/TNW, and K/TNW were calculated to be 3.25, 3.15, 3.04 and 2.94 eV respectively. The red shift as alkali strength is increased may be due to the narrowing of the slimming of the nanowires [34,34] as it may be associated with increased redox abilities for the production of photogenerated electron-hole pairs and reduced recombination effect in photocatalytic systems[35].

Effect of operating variables

The effect of TiO$_2$ loading and the initial concentration of MB, and their impacts on the degradation of MB were investigated using the central composite design (CCD) approach and response data were analyzed using Design-Expert version 6.0.6. The results for degradation over Na/TNW and K/TNW fit quadratic model equations (3) and (4), respectively. Each coefficient of the variable in the equation estimates the change in mean response per unit increase in the associated independent variable when the other variable is held constant.

$$\%D = 57.37 + 2.57[TiO_2] - 15.7[TiO_2]^2 - 9.65[MB]^2 \qquad (3)$$

$$\%D = 65.83 + 3.03[MB] - 20.47[TiO_2]^2 - 7.32[MB]^2 - 9.08[TiO_2][MB] \qquad (4)$$

The predicted MB degradation efficiencies (%D) in the presence of Na/TNW and K/TNW are presented in Table 2. It can be seen from the table for both catalysts that a good correlation exists between the experimental and predicted % degradation. This is affirmed by the linear normal plot of residuals (Fig. 10), in which normal probabilities correlate well with residuals. The residuals analysis accounts for the difference between the observed and the predicted response value, thus giving useful information about the model goodness of fit. The plot of normal probability of the residual for MB degradation (Fig.10) reveals a reasonably well-behaved residual of MB degradation as the majority of the points lie on a straight line. Hence the estimated effects are real and differ markedly from noise [36,26].

The statistical significance of the CCD model was assessed by ANOVA. A summary of the probability criteria and results of the F-test for Na/TNW and K/TNW assisted processes are tabulated in Table 3. The models' Prob > F and those of the terms in the hierarchy of the model equation are less than 0.05 which shows that predicted degradation efficiencies are not influenced at 95 % confidence level. In an experiment, the minimum adequate precision desirable is a value > 4. In this study, the adequate precision for the Na/TNW and K/TNW models are 21.316 and 28.981 (Table A4 and A5 of supplementary materials), respectively. The models also show extremely low standard deviation from the mean degradation efficiency.

Table 2. The bivariate experimental design matrix and corresponding degradation efficiencies in the presence of Na/TNW and K/ TNW.

| Run	TiO₂ (g/L)	[MB] (mg/l)	%D_Experimental	%D_Predicted	%D_Experimental	%D_Predicted
			In the presence of Na/TNW		In the presence of K/TNW	
1	0.6	25	56.10	57.37	66.90	65.83
2	1	25	32.30	29.61	28.70	26.26
3	0.4	30	27.60	26.70	49.50	49.18
4	0.8	20	30.20	33.45	42.80	45.96
5	0.2	25	22.00	22.34	23.00	23.52
6	0.6	15	41.80	39.21	48.20	46.90
7	0.4	20	31.10	32.21	24.80	24.96
8	0.6	25	57.30	57.37	64.80	65.83
9	0.6	25	58.70	57.37	65.80	65.83
10	0.8	30	34.50	35.74	31.20	32.97
11	0.6	35	36.70	36.94	56.10	55.48
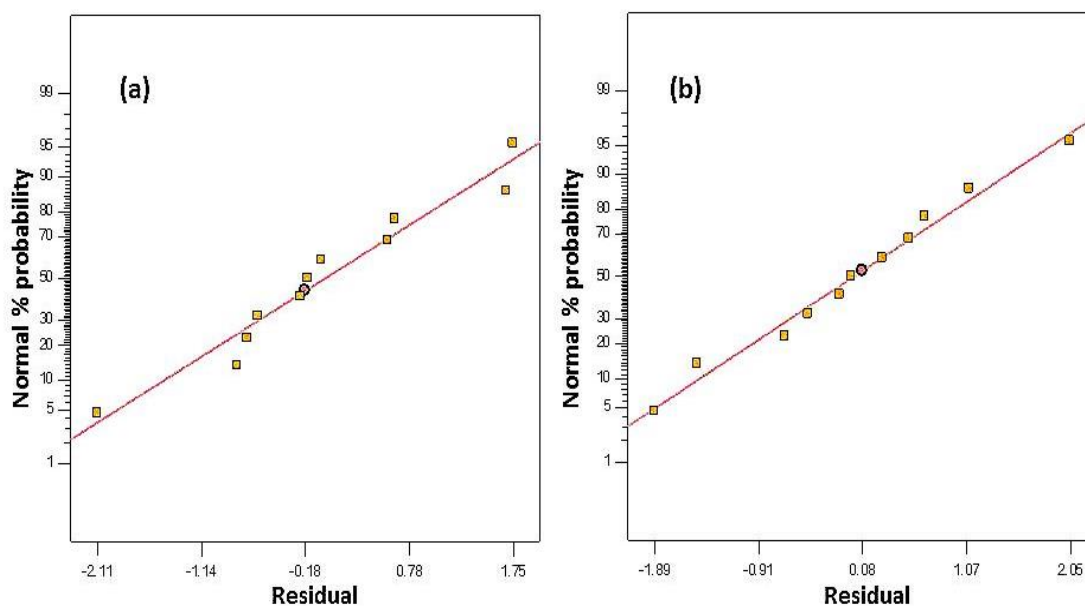
Fig. 10. Normal probability with residual values of the photo-oxidative degradation process over (a) Na/TNW and (b) K/TNW.

This confirms that the obtained models can be successfully used to navigate the design space.

Numerical optimization was conducted to obtain the maximum performance of the variables necessary. The theoretical value of removable MB from reaction medium was 57.4827 % in presence of 0.616 g/l Na/TNW and 24.85 mg/l [MB], with desirability factor of 0.967, whereas and 66.1593 % [MB] can be removed in presence of 0.594 g/l K/ TNW and 26.1 mg/l [MB], with desirability factor

of 0.983, respectively.

The effects of catalyst loading and initial MB concentration are depicted by the three-dimensional response surfaces shown in Fig. 11. It can be seen that, for both Na/TNW (Fig. 11A) and K/TNW (Fig. 11B), there is synergy between [TiO₂] and [MB] as they are increased towards 0.6 g/L and 20 mg/l (corresponding to the experimental optimum). The maximum degradation efficiency of 57.37 % for Na/TNW and 65.83% for K/TNW

Table 3. Results of ANOVA (p-value and F-value) for MB degradation over the nanowires.

Source	MB Removal over Na/TNW		MB Removal over K/TNW	
	F-Value	Prob>F	F-Value	Prob>F
Model	71.84	<0.0001	158.28	<0.0001
A	7.12	0.0321	*NA	*NA
B	*NA	*NA	16.77	0.0064
A^2	187.35	<0.0001	538.96	<0.0001
B^2	70.76	0.0001	68.95	0.0002
AB	*NA	*NA	75.01	0.0001
Lack of Fit	5.74	0.1550	5.02	0.1706

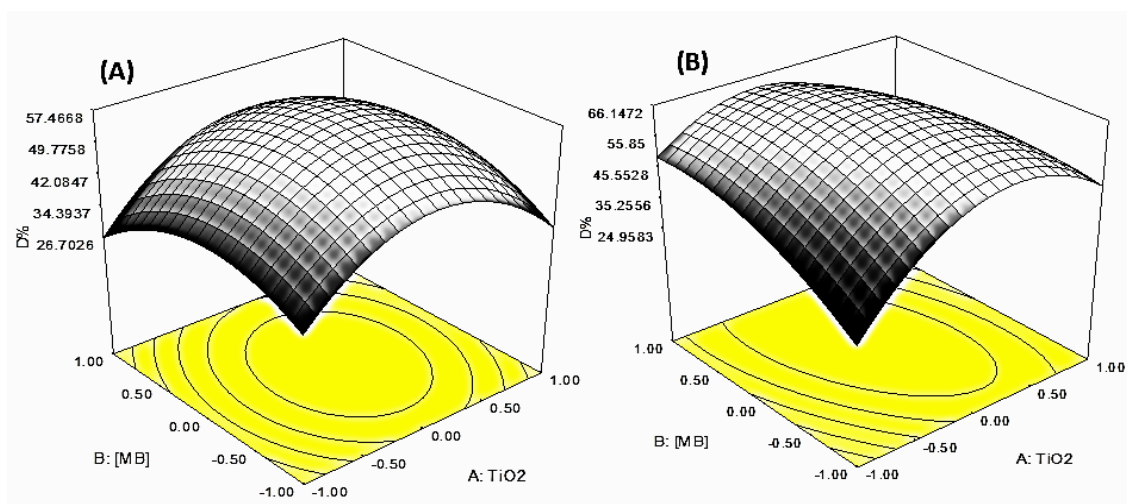*Not applicable because the term does not exist in the hierarchy.

Fig. 11. The response surface of MB degradation as a function of [TiO₂] and [MO] for (A) Na/TNW and (B) K/TNW.

is reached in 60 min. The figure reveals that alternating any of the combinations of levels would result in low degradation efficiency. The coefficients of model terms, suggests that TiO₂ loading has positive impact on degradation efficiency of MB for both Na/TNW and K/TNW while the initial MB concentration has negative effect for Na/TNW and positive effect for K/TNW. The model terms showed negative impact with respect to quadratic coefficient for both Na/TNW and K/TNW.

To validate the results obtained by the models and to confirm the models competence for predicting maximum degradation of MB, three experiments were conducted using the optimum conditions, which yielded an average maximum MB degradation of 56.98 % and 65.77 for Na/TNW and K/TNW respectively and the average values

were calculated (predicted values) which is found to be 57.02 (for Na/TNW) and 65.80 (for K/TNW). The results show that it is feasible to predict and optimize the MB photocatalytic degradation using response surface methodology.

Photocatalytic kinetics

To obtain relevant information about the photocatalytic performance, it is necessary to perform experiments from which any possible contributions from direct photolysis or adsorptive removal can be excluded. In this regard, experiments were performed under UV irradiation in the absence of TiO₂ and in the dark with TiO₂ photocatalyst for 100 min and the results are displayed by Fig. 12. It can be seen from the figure that the least catalytic performance was obtained with P25 (77.12 %) while K/TNW was found to
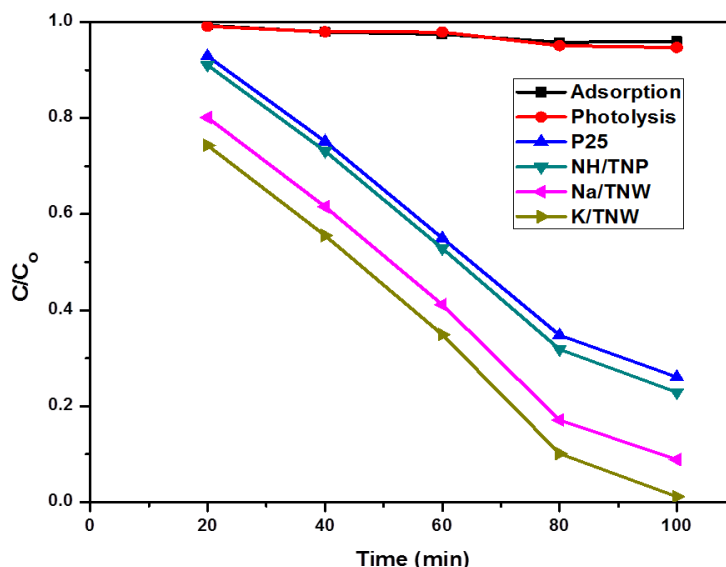
Fig. 12. Photocatalytic degradation of MB in presence of the obtained photocatalysts under UV irradiation for 100 min.
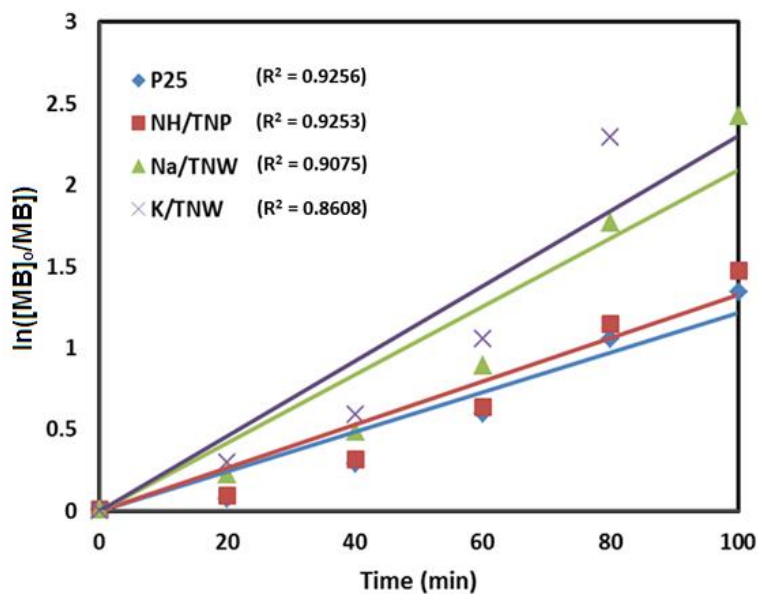

Fig. 13. Pseudo-first-order graph of MB degradation.

have the highest catalytic performance (98.87%). These results correlate well with the BET and UV-Vis results which showed better MB removal as surface area of K/TNW is increased or its band gap is decreased.

The degradation of MB carried out in this study (Fig. 13) was fitted into the pseudo-first-order kinetics represented by Eq. (6).

$$\ln(\frac{[MB]_o}{[MB]_t}) = kt \qquad (6)$$

where $[MB]_t$ and $[MB]_o$ is the concentration (mg/l) at time t and when t = 0 respectively and k is the apparent reaction rate constant (expressed as min^{-1}). A plot of $\ln([MO]_o/[MO]_t)$ versus t gave a straight line with slope = k with R square values > 0.85 (Fig. 13).

CONCLUSION

The effect of alkali strength on the hydrothermal

growth of TiO$_2$ nanowires was successfully investigated. The hydrothermal treatment with weak base does not affect the morphology of the TiO$_2$ and does not form nanowires, but can result in its downsizing. However, the hydrothermal treatment of TiO$_2$ with strong alkalis leads to TiO$_2$ nanowires with relatively controllable, narrower diameter, higher surface area, and narrower band gap energy.

ACKNOWLEDGMENTS

CONFLICT OF INTEREST

The authors declare that there are no conflicts of interest regarding the publication of this manuscript.

REFERENCES

1. Ahmadian-Fard-Fini S, Ghanbari D, Amiri O, Salavati-Niasari M. Electro-spinning of cellulose acetate nanofibers/Fe/carbon dot as photoluminescence sensor for mercury (II) and lead (II) ions. Carbohydrate Polymers. 2020;229:115428.

2. Bagheri A, Halakouie H, Ghanbari D, Mousayi M, Asiabani N. Strontium hexa-ferrites and polyaniline nanocomposite: Studies of magnetization, coercivity, morphology and microwave absorption. J. Nanostruct. 2019; 9(4):630-638.

3. Nabiyouni G, Ghanbari D. Simple preparation of magnetic, antibacterial and photo-catalyst NiFe$_2$O$_4$@TiO$_2$/Pt nanocomposites. J. Nanostruct. 2018; 8(4):408-416.

4. Kiani A, Nabiyouni G, Masoumi S, Ghanbari D. A novel magnetic MgFe2O4–MgTiO3 perovskite nanocomposite: Rapid photo-degradation of toxic dyes under visible irradiation. Composites Part B: Engineering. 2019;175:107080.

5. Eskandari N, Nabiyouni G, Masoumi S, Ghanbari D. Preparation of a new magnetic and photo-catalyst CoFe2O4–SrTiO3 perovskite nanocomposite for photo-degradation of toxic dyes under short time visible irradiation. Composites Part B: Engineering. 2019;176:107343.

6. Sorinezami Z, Ghanbari D. Facile preparation of silver nanoparticles and antibacterial chitosan-Ag polymeric nanocomposites. J. Nanostruct. 2019; 9(3):396-401.

7. Singh R, Bapat R, Qin L, Feng H, Polshettiwar V. Atomic Layer Deposited (ALD) TiO2 on Fibrous Nano-Silica (KCC-1) for Photocatalysis: Nanoparticle Formation and Size Quantization Effect. ACS Catalysis. 2016;6(5):2770-84.

8. Haider Z, Kang YS. Facile Preparation of Hierarchical TiO2 Nano Structures: Growth Mechanism and Enhanced Photocatalytic H2 Production from Water Splitting Using Methanol as a Sacrificial Reagent. ACS Applied Materials & Interfaces. 2014;6(13):10342-52.

9. Naik B, Moon SY, Kim SH, Park JY. Enhanced photocatalytic generation of hydrogen by Pt-deposited nitrogen-doped TiO2 hierarchical nanostructures. Applied Surface Science. 2015;354:347-52.

10. Liu J, Li Y, Ke J, Wang S, Wang L, Xiao H. Black NiO-TiO$_2$ nanorods for solar photocatalysis: Recognition of electronic structure and reaction mechanism. Appl. Catal. B, 2018; 224:705-714. 9. Shao J, Sheng W, Wang M, Li S, Chen J, Zhang Y, Cao S. In situ synthesis of carbon-doped TiO$_2$ single-crystal nanorods with a remarkably photocatalytic efficiency. Appl. Catal. B, 2017; 209:311-314. Haider Z, Kang YS. Facile preparation of hierarchical TiO$_2$ nano structures: growth mechanism and enhanced photocatalytic H$_2$ production from water splitting using methanol as a sacrificial reagent. ACS Applied Materials & Interfaces. 2014;6(13):10342-52.

11. Zhang Y, Han C, Zhang G, Dionysiou DD, Nadagouda MN. PEG-assisted synthesis of crystal TiO2 nanowires with high specific surface area for enhanced photocatalytic degradation of atrazine. Chemical Engineering Journal. 2015;268:170-9.

12. Zhang Y, Han C, Zhang G, Dionysiou DD, Nadagouda MN. PEG-assisted synthesis of crystal TiO2 nanowires with high specific surface area for enhanced photocatalytic degradation of atrazine. Chemical Engineering Journal. 2015;268:170-9.

13. Wahi RK, Liu Y, Falkner JC, Colvin VL. Solvothermal synthesis and characterization of anatase TiO2 nanocrystals with ultrahigh surface area. Journal of Colloid and Interface Science. 2006;302(2):530-6.

14. Yang J, Du J, Li X, Liu Y, Jiang C, Qi W, et al. Highly Hydrophilic TiO2 Nanowires Network by Alkaline Hydrothermal Method for Photocatalysis Degradation of Methyl Orange. Nanomaterials. 2019;9(4):526.

15. Yang J, Du J, Li X, Liu Y, Jiang C, Qi W, et al. Highly Hydrophilic TiO2 Nanowires Network by Alkaline Hydrothermal Method for Photocatalysis Degradation of Methyl Orange. Nanomaterials. 2019;9(4):526.

16. Erdogan N, Park J, Choi W, Kim SY, Ozturk A. Alkaline Hydrothermal Synthesis, Characterization, and Photocatalytic Activity of TiO2 Nanostructures: The Effect of Initial TiO2 Phase. Journal of Nanoscience and Nanotechnology. 2019;19(3):1511-9.

17. Bazargan MH, Byranvand MM, Kharat AN. Preparation and characterization of low temperature sintering nanocrystalline TiO2prepared via the sol-gel method using titanium(IV) butoxide applicable to flexible dye sensitized solar cells. International Journal of Materials Research. 2012;103(3):347-51.

18. Shinde PS, Bhosale CH. Properties of chemical vapour deposited nanocrystalline TiO2 thin films and their use in dye-sensitized solar cells. Journal of Analytical and Applied Pyrolysis. 2008;82(1):83-8.

19. Corradi AB, Bondioli F, Focher B, Ferrari AM, Grippo C, Mariani E, et al. Conventional and Microwave-Hydrothermal Synthesis of TiO2 Nanopowders. Journal of the American Ceramic Society. 2005;88(9):2639-41.

20. Zulfiqar M, Chowdhury S, Omar AA. Hydrothermal synthesis of multiwalled TiO2 nanowires and its photocatalytic activities for Orange II removal. Separation

Science and Technology. 2018;53(9):1412-22.

21. Camposeco R, Castillo S, Navarrete J, Gomez R. Synthesis, characterization and photocatalytic activity of TiO2 nanostructures: Nanowires, nanofibers, nanowires and nanoparticles. Catalysis Today. 2016;266:90-101.

22. Al-Hajji LA, Ismail AA, Al-Hazza A, Ahmed SA, Alsaidi M, Almutawa F, et al. Impact of calcination of hydrothermally synthesized TiO2 nanowires on their photocatalytic efficiency. Journal of Molecular Structure. 2020;1200:127153.

23. Jitputti J, Suzuki Y, Yoshikawa S. Synthesis of TiO2 nanowires and their photocatalytic activity for hydrogen evolution. Catalysis Communications. 2008;9(6):1265-71.

24. Jawad AH, Alkarkhi AFM, Mubarak NSA. Photocatalytic decolorization of methylene blue by an immobilized TiO2 film under visible light irradiation: optimization using response surface methodology (RSM). Desalination and Water Treatment. 2014;56(1):161-72.

25. Zhang YX, Li GH, Jin YX, Zhang Y, Zhang J, Zhang LD. Hydrothermal synthesis and photoluminescence of TiO2 nanowires. Chemical Physics Letters. 2002;365(3-4):300-4.

26. Zhou X, Liu N, Schmuki P. Photocatalysis with TiO2 Nanowires: "Colorful" Reactivity and Designing Site-Specific Photocatalytic Centers into TiO2 Nanowires. ACS Catalysis. 2017;7(5):3210-35.

27. Cano-Casanova L, Amorós-Pérez A, Ouzzine M, Lillo-Ródenas MA, Román-Martínez MC. One step hydrothermal synthesis of TiO2 with variable HCl concentration: Detailed characterization and photocatalytic activity in propene oxidation. Applied Catalysis B: Environmental. 2018;220:645-53.

28. Zhong JS, Wang QY, Zhu X, Chen DQ, Ji ZG. Sovolthermal synthesis of flower-like Cu3BiS3 sensitized TiO2 nanowire arrays for enhancing photoelectrochemical performance.

Journal of Alloys and Compounds. 2015;641:144-7.

29. Zhu Z, Lin S-J, Wu C-H, Wu R-J. Synthesis of TiO2 nanowires for rapid NO2 detection. Sensors and Actuators A: Physical. 2018;272:288-94.

30. Makal P, Das D. Self-doped TiO2 nanowires in TiO2-B single phase, TiO2-B/anatase and TiO2-anatase/rutile heterojunctions demonstrating individual superiority in photocatalytic activity under visible and UV light. Applied Surface Science. 2018;455:1106-15.

31. Ba-Abbad MM, Kadhum AAH, Mohamad AB, Takriff MS, Sopian K. Photocatalytic degradation of chlorophenols under direct solar radiation in the presence of ZnO catalyst. Research on Chemical Intermediates. 2012;39(5):1981-96.

32. López R, Gómez R. Band-gap energy estimation from diffuse reflectance measurements on sol–gel and commercial TiO2: a comparative study. Journal of Sol-Gel Science and Technology. 2011;61(1):1-7.

33. Ba-Abbad MM, Kadhum AAH, Mohamad AB, Takriff MS, Sopian K. Synthesis and catalytic activity of TiO₂ nanoparticles for photochemical oxidation of concentrated chlorophenols under direct solar radiation. Int. J. Electrochem. Sci., 2012; 7(6):4871-4888.

34. Nam CT, Falconer JL, Duc LM, Yang W-D. Morphology, structure and adsorption of titanate nanowires prepared using a solvothermal method. Materials Research Bulletin. 2014;51:49-55.

35. Zhao X, Wu P, Liu M, Lu D, Ming J, Li C, et al. Y2O3 modified TiO2 nanosheets enhanced the photocatalytic removal of 4-chlorophenol and Cr (VI) in sun light. Applied Surface Science. 2017;410:134-44.

36. Alidokht L, Khataee AR, Reyhanitabar A, Oustan S. Cr(VI) Immobilization Process in a Cr-Spiked Soil by Zerovalent Iron Nanoparticles: Optimization Using Response Surface Methodology. CLEAN - Soil, Air, Water. 2011;39(7):633-40.